Nanoscale

PAPER

View Article Online
View Journal

Cite this: DOI: 10.1039/c7nr03740f

Tuning the coercivity and exchange bias by controlling the interface coupling in bimagnetic core/shell nanoparticles†

Gabriel C. Lavorato, Enio Lima, Jr., Horacio E. Troiani, Roberto D. Zysler and Elin L. Winkler *

Received 25th May 2017,
Accepted 10th June 2017

DOI: 10.1039/c7nr03740f

rsc.li/nanoscale

In order to explore an alternative strategy to design exchange-biased magnetic nanostructures, bimagnetic core/shell nanoparticles have been fabricated by a thermal decomposition method and systematically studied as a function of the interface exchange coupling. The nanoparticles are constituted by a ~3 nm antiferromagnetic (AFM) CoO core encapsulated in a ~4 nm-thick $Co_{1-x}Zn_xFe_2O_4$ (x = 0–1) ferrimagnetic (FiM) shell. The system presents an enhancement of the coercivity (H_C) as compared to its FiM single-phase counterpart and exchange bias fields (H_{EB}). While H_C decreases monotonically with the Zn concentration from ~21.5 kOe for x = 0, to ~7.1 kOe for x = 1, H_{EB} exhibits a non-monotonous behavior being maximum, H_{EB} ~ 1.4 kOe, for intermediate concentrations. We found that the relationship between the AFM anisotropy energy and the exchange coupling energy can be tuned by replacing Co^{2+} with Zn^{2+} ions in the shell. As a consequence, the magnetization reversal mechanism of the system is changed from an AFM/FiM rigid-coupling regime to an exchange-biased regime, providing a new approach to tune the magnetic properties and to design novel hybrid nanostructures.

1. Introduction

The control of exchange-coupling at the interface of bimagnetic nanostructures has guided in the past few decades the fabrication of new magnetic materials with an outstanding technological impact. Exchange-biased layers enabled the development of spin valves and magnetoresistive multilayers[1,2] and exchange-spring phenomena provided a new framework for the improvement of permanent magnets.[3,4] In the last few years, the interface-coupling has been proposed as a mechanism for enhancing the thermal stability of nanoparticles for recording media,[5,6] for designing efficient nanoheaters for hyperthermia,[7] and for increasing the energy product of nanocomposite magnets.[8]

Exchange bias (EB) phenomena were first studied in ferromagnetic (FM)-/antiferromagnetic (AFM)-Co/CoO nanoparticles[9] and have been extensively investigated in many hybrid materials.[10,11] In AFM/FM heterostructures, the EB is typically manifested by a field-shift (H_{EB}) in the hysteresis loop after cooling the material in a magnetic field from temperatures higher than the Néel temperature of the AFM (T_N) and lower than the Curie temperature of the FM (T_C), and is also related to other features *e.g.* unidirectional anisotropy,[12] effective anisotropy increase[9,13] or asymmetric loops.[10,14] The physical origin of EB is usually explained by describing the magnetization reversal mechanism in terms of the exchange-coupling between the AFM and the FM (or ferrimagnetic – FiM) spins at the interface.[9,10,15] The ratio between the interface coupling energy and the anisotropy energy of the AFM determines the coupling regime and the magnetization reversal mechanism. In this simple interpretation, when the interface coupling energy is much larger than the antiferromagnetic anisotropy energy, a rigid AFM–FM(FiM) coupling is expected and a significant increase in the effective anisotropy, with the consequent enhancement of the coercive field (H_C), is usually observed. Conversely, when the anisotropy energy is much stronger than the interface coupling energy, exchange-biased loops are typically observed. The presence of H_{EB} is associated with the pinning action exerted by the AFM phase over the FM(FiM) spins, which induces an extra torque to the magnetization reversal process.[10]

Although first studied in nanoparticles, most of the research studies on EB have been focused on thin films as a result of the difficulties in the fabrication of bimagnetic nanoparticles with controlled size, morphology and composition. However, great progress in the fabrication routes achieved during the last few years,[16–18] prompted numerous systematic

Centro Atómico Bariloche, CNEA-CONICET, Av. Bustillo 9500, Bariloche, Río Negro, Argentina. E-mail: winkler@cab.cnea.gov.ar; Tel: +54 294 4445158

†Electronic supplementary information (ESI) available. See DOI: 10.1039/C7NR03740F

studies on exchange-coupled nanoparticle-based bimagnetic systems, including FM(FiM)-core/AFM-shell,[13,19,20] FM-core/FiM-shell,[21] hard/soft FiM-core/FiM-shell,[6,22] inverted AFM-core/FiM-shell,[23,24] doubly inverted AFM-core/FiM-shell ($T_N > T_C$)[25] and multi-shell nanoparticles.[26] Most of the previous studies on core/shell nanoparticles have been focused on tuning H_{EB} and H_C by controlling the size of the core and shell components[25,27–31] or by introducing materials with different magnetic anisotropies.[32,33] However, although predicted by Monte Carlo simulations,[34,35] the possibility of adjusting directly the interface exchange-coupling energy has not been explored experimentally and could offer a new tool to control the magnetic response of hybrid nanoparticles.

Recently, we have shown that $CoO/CoFe_2O_4$ nanoparticles present a remarkable increase in the low temperature coercivity due to the exchange coupling at the interface.[24] Such an increased effective anisotropy is originated by a very high interface exchange interaction that promotes a rigid-coupling regime[36] and no sign of EB was observed in such systems, even for 5 nm $CoO/CoFe_2O_4$ nanoparticles with a thin (≤2 nm) shell.[37] In this work, we show that H_C and H_{EB} can be simultaneously tuned by controlling the interface exchange coupling energy. With this aim we fabricated and systematically studied $CoO/Co_{1-x}Zn_xFe_2O_4$ (x = 0–1) core/shell nanoparticles with a ~3 nm core and a total diameter of ~10–12 nm. By doping the FiM phase with non-magnetic Zn atoms a decrease in the interface coupling energy is promoted, which is responsible for the Zn concentration-dependence of H_{EB} and H_C. This approach can be used to tune the specific magnetic properties of AFM/FiM nanostructures at the crossover between rigid-coupling and exchange-biased magnetization reversal mechanisms.

2. Experimental

$CoO/Co_{1-x}Zn_xFe_2O_4$ core/shell nanoparticles were fabricated by high temperature decomposition of metal-acetylacetonates in diphenyl ether assisted by oleic acid and oleylamine by modifying the method proposed in ref. 38. In a typical synthesis, precursors, solvents and surfactants are mixed in a three-neck 250 mL flask, under an N_2 atmosphere, equipped with a water-refrigerated condenser. Monodisperse CoO cores were obtained by mixing 1.5 mmol of Co(II) acetylacetonate ($Co(acac)_2$) with a long-chain alcohol 1,2-octanediol (1 mmol), diphenyl ether (94 mmol), oleic acid (3 mmol), and oleylamine (3 mmol). The mixture was heated at a rate of 8 °C min^{-1} to the reflux temperature (260 °C) for a total time of 120 min. Once cooled down to room temperature, in order to grow the spinel ferrite on the CoO seeds, Zn(II) acetylacetonate ($Zn(acac)_2$), Fe(III) acetylacetonate ($Fe(acac)_3$) and $Co(acac)_2$ (total organometallic precursors of 0.9 mmol), together with 1,2-octanediol (1 mmol), oleic acid (1.5 mmol), oleylamine (1.5 mmol) and diphenyl ether (47 mmol) were added to the mixture and the heating procedure was repeated using a slightly higher heating rate (12 °C min^{-1}) in order to avoid homogeneous nucleation and the mixture was maintained under reflux for 120 min. In this step, metal-acetylacetonates were added according to a nominal molar ratio of $Co_{1-x}Zn_xFe_2O_4$. For example, $CoO/Zn_{0.5}Co_{0.5}Fe_2O_4$ nanoparticles were fabricated by adding 0.15 mmol of $Zn(acac)_2$, 0.15 mmol of $Co(acac)_2$ and 0.6 mmol of $Fe(acac)_3$. Five $CoO/Co_{1-x}Zn_xFe_2O_4$ samples were produced by changing the Zn : Co ratio, where the nominal Zn atomic fraction x was fixed at 0, 0.25, 0.5, 0.75 and 1, and were labeled as Zn-0, Zn-0.25, Zn-0.5, Zn-0.75 and Zn-1, respectively. The as-prepared nanoparticles were extracted and washed several times, where each step consists of addition of ethanol : hexane solution (8 : 1) followed by centrifugation (14 000 rpm/30 min). The precipitated nanoparticles were dried and annealed at 300 °C under an air atmosphere for 120 min with a fixed heating rate of 3 °C min^{-1}. The annealed samples can be re-dispersed in hexane or toluene after sonication for 1 h. A thermogravimetric analysis (TGA, Shimadzu DTG-60H) performed by recording the mass of the samples after heating up to 600 °C suggests that a residual organic coating in the range 9–14% of the total mass is preserved after the thermal treatment. The nature of such a residual organic layer was evaluated by Fourier transform infrared spectroscopy (FT-IR) performed on a PerkinElmer Spectrum Two IR spectrometer using the UATR (single reflection diamond) optical path.

Structural characterization was performed by conducting X-ray diffraction (XRD) experiments on a PANAlytical X'Pert diffractometer with Cu Kα radiation using a glass sample holder (step size 0.026°, range 17–80°). The crystallite size was estimated from the broadening of the X-ray diffraction peaks by the Scherrer expression $D = \lambda K/(\beta_{hkl}\cos(\theta_{hkl}))$, where D is the mean crystallite equivalent diameter, K is a constant that depends on the nanocrystal shape (usually $K \sim 0.89$), λ is the wavelength of the X-rays and β_{hkl} is the full width at half maximum of the reflection associated with the angle θ_{hkl}. The core/shell morphology, the particle size and the size dispersion were evaluated using a transmission electron microscope (TEM, Philips CM200 operated at 200 kV, with an Ultra-Twin lens and a resolution of 0.19 nm). The size dispersion of each sample was analyzed by measuring ~200 particles from TEM micrographs and constructing the corresponding histograms that were fitted with a lognormal function: $f(D) = (\sqrt{2\pi}\sigma D)^{-1} e^{-\ln^2(D/D_0)/2\sigma^2}$. From the fit, the mean particle size, $\langle D_{NP}\rangle = D_0 e^{\sigma^2/2}$, and its standard deviation, $\sigma_{NP} = \langle D_{NP}\rangle\sqrt{e^{\sigma^2} - 1}$, were computed.

In order to prevent the mechanical movement of the nanoparticles during the magnetic experiments, the annealed particles dispersed in hexane were mixed with an epoxy resin. After evaporation of the hexane, the resin was cured by adding the hardener component and placing it in a gelatin capsule. Being transferred from the solvent, the nanoparticles in the resin composite are expected to keep the same dispersion degree. The magnetic properties were studied using a SQUID magnetometer (MPMS Quantum Design) with a maximum applied field of ±50 kOe. Zero-field cooled (ZFC) and field-

cooled (FC, from 310 K with an applied field of 10 kOe) hysteresis loops were recorded at 5 K and the temperature dependence of the magnetization was analyzed in the range of 5–330 K by measuring the ZFC and FC curves with an applied field of 50 Oe.

3. Results and discussion

3.1. Structural and morphological characterization

CoO cores encapsulated in a Zn–Co ferrite with reproducible characteristics were successfully synthesized by employing a two-step high-temperature decomposition method. Being encapsulated in the ferrite, the CoO is expected to be protected against oxidation,[39,40] which is critical for the observation of interface-dependent magnetic phenomena.

The XRD patterns of bare cores and core/shell nanoparticles are shown in Fig. 1. The former consists of broad peaks associated with a nanosized phase indexed with bulk CoO (JCPDS-ICDD card no. 43-1004) and the average crystallite size calculated by using the Scherrer formula, 3 nm, is in agreement with the mean size estimated from the TEM images (see Fig. 2). From the XRD patterns of core/shell nanoparticles only spinel-type reflections are detected at first sight, probably due to the peak broadening of the CoO phase and the relative intensities of both phases. The expected bulk reflections for $CoFe_2O_4$ (JCPDS-ICDD card no. 22-1086) are indicated for sample Zn-0.

The lattice parameter for each composition of the spinel ferrite (a_{ZCFO}), evaluated from the position of XRD peaks, is slightly shifted to lower values with the Zn incorporation, as summarized in Table 1. Although the lattice parameter for bulk $ZnFe_2O_4$ is expected to be higher than that for $CoFe_2O_4$ (a_{ZFO} = 8.42 Å and a_{CFO} = 8.39 Å), it has been shown that imperfections and cation mixing (partial inversion) in Zn–ferrite nanoparticles promote a lower lattice parameter.[41,42] As it is discussed below, the high magnetization observed for CoO/$ZnFe_2O_4$ nanoparticles reinforces this assumption.

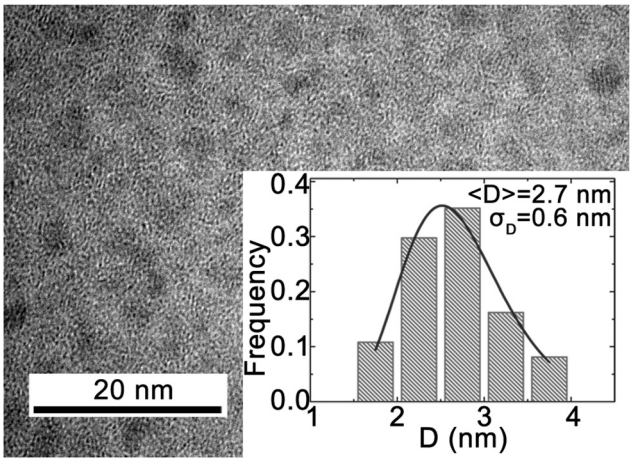

Fig. 2 Transmission electron micrograph of bare CoO nanoparticles. The inset shows the size distribution histogram fitted by a lognormal function (the mean value and standard deviation of the fit are indicated in the graph).

Table 1 Summary of the structural characterization of CoO/$Co_{1-x}Zn_xFe_2O_4$ nanoparticles (samples Zn-*x*): nominal Zn fraction (x_{NOM}), mean nanoparticle diameter ($\langle D_{NP}\rangle$) and its standard deviation (σ_{NP}) obtained from the TEM images and lattice parameter of the ferrite (a_{ZCFO})

Sample	x_{NOM}	$\langle D_{NP}\rangle$ (nm)	σ_{NP} (nm)	a_{ZCFO} (Å)
Zn-0	0	12.0	2.1	8.34(1)
Zn-0.25	0.25	10.0	1.5	8.29(2)
Zn-0.5	0.5	10.5	1.6	8.29(2)
Zn-0.75	0.75	11.7	2.0	8.30(1)
Zn-1	1	10.4	1.7	8.28(2)

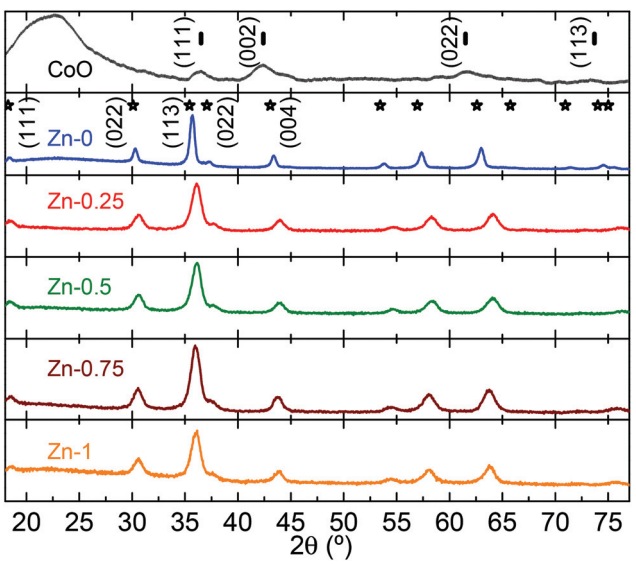

Fig. 1 X-ray diffraction patterns for bare CoO and CoO/$Co_{1-x}Zn_xFe_2O_4$ (x = 0–1) core/shell nanoparticles (samples Zn-*x*). The bars and stars indicate the positions of bulk CoO and $CoFe_2O_4$ reflections, respectively.

The size and morphology of the nanoparticles were further analyzed from the TEM images. Fig. 3 shows representative bright-field and high resolution images that were employed to evaluate the size dispersion and a mean particle size between 10 and 12 nm was found for all the samples (see Table 1). From the high-resolution TEM images, shown in Fig. 3f–j, it is possible to distinguish different crystallographic orientations for the core and shell. Interestingly, the shell is formed by several ferrite grains in close contact, similarly to the reported morphology for other core/shell[24] and hollow[43] nanoparticles. The dark-field images, shown in Fig. S1,† confirm the core/shell structure with a ~3–4 nm thick ferrite shell for all samples.

The presence of a residual organic coating after the annealing, already observed in previous studies of nanoparticles synthesized by similar chemical routes,[44–46] was evaluated by HRTEM and FT-IR measurements. The HRTEM images

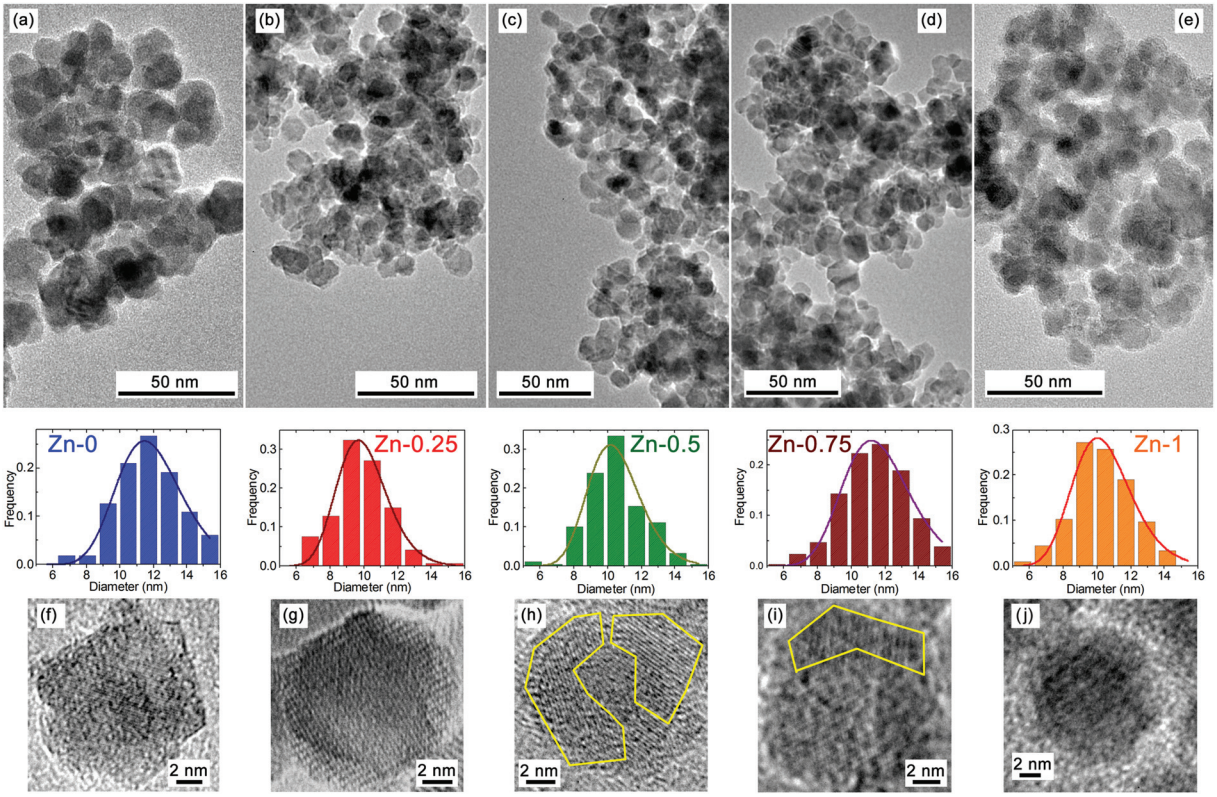

Fig. 3 (a–e) Transmission electron micrographs with their corresponding size histograms (fitted with a lognormal function) and (f–j) high resolution TEM images of $CoO/Co_{1-x}Zn_xFe_2O_4$ (x = 0–1) core/shell nanoparticles (samples Zn-x).

(Fig. S2†) show that the annealed core/shell nanoparticles are covered by an organic layer of ~2 nm that prevents their coalescence (further details can be found in the ESI†). Consistently, the FT-IR spectra reveal that the characteristic C–H, CH_3 and the –COO– stretching absorptions bands of oleic acid are still present after the annealing (Fig. S3†). Moreover, in agreement with previous results,[45,47] the chemical bonding between the carboxyl group of the oleic acid and the metal atoms of the nanoparticles is confirmed by the absence of the C=O stretching vibration of the carboxyl group, characteristic of the free oleic acid.

3.2. Magnetic properties

Once the size and morphology of the nanoparticles were determined, we focus on the ZFC and FC low temperature hysteresis loops presented in Fig. 4. As a first concern, the saturation magnetization (M_S) is similar for Zn-0 and Zn-1, and is slightly reduced for intermediate Zn concentrations. It is known that the magnetic properties of ferrites, such as transition temperature and saturation magnetic moment, strongly depend on the cation distribution at the tetrahedral (A) and octahedral (B) sites of the AB_2O_4 spinel. Bulk $ZnFe_2O_4$, for example, crystallizes in a normal spinel structure (tetrahedral A sites occupied by Zn^{2+} atoms) and it is ordered antiferromagnetically at T_N ~ 10 K;[48] however, the amount of Zn^{2+} in tetrahedral sites is usually reduced when the size decreases, and then the nanoparticles show an increased inversion degree which leads to the stabilization of the ferrimagnetic order.[49–51] This is because the AFM order in the normal spinel is determined by the weak AFM superexchange interaction between the B sites, while in the inverted structure the strong superexchange interaction between Fe^{3+} located at the A and B sites stabilizes the

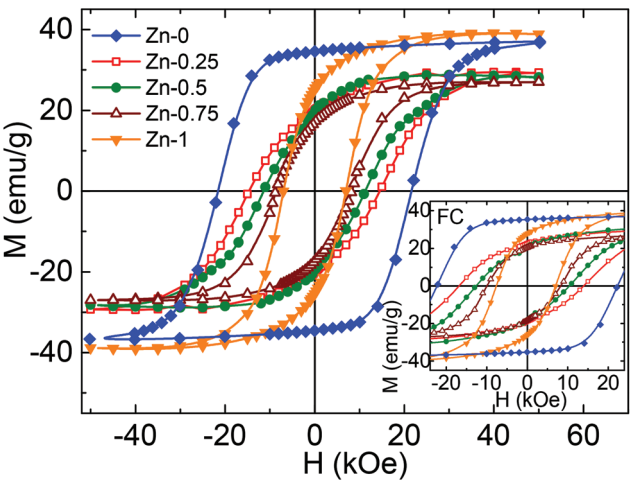

Fig. 4 Zero-field-cooled and (inset) field-cooled (from 310 K with 10 kOe) hysteresis loops of $CoO/Co_{1-x}Zn_xFe_2O_4$ (x = 0–1) core/shell nanoparticles (samples Zn-x) measured at 5 K.

FiM order at higher temperatures. Therefore, the morphology of the shell, composed by small nanograins of ferrites, is likely to favor the formation of inverted structures and the ferrites with a high Zn concentration show larger M_S values compared to their bulk counterpart.[52–54] As a result, the saturation magnetization of the core/shell nanoparticles does not change significantly with the Zn concentration and remains in the 28–38 emu g_{NPs}^{-1} range.

The coercivity (H_C) and the exchange bias shift (H_{EB}) obtained from the ZFC and FC hysteresis loops measured at 5 K are summarized in Table 2 and Fig. 5. While H_C monotonically decreases from 21.5 kOe to 7.1 kOe when increasing the Zn content, H_{EB} presents a maximum for $x = 0.25$. When Co^{2+} is substituted by Zn^{2+} in the spinel structure a reduction in the magnetocrystalline anisotropy of the ferrite is expected. In fact, previous reports have shown that the low temperature H_C of 5–12 nm Zn–Co ferrite nanoparticles is reduced from 7–15 kOe for $CoFe_2O_4$ to 0.06–0.1 kOe for $ZnFe_2O_4$.[52,53,55] However, the H_C of $CoO/Co_{1-x}Zn_xFe_2O_4$ nanoparticles is much larger than the value reported for the associated single-phase Zn–Co ferrites. Such an H_C enhancement cannot be explained only by the increased surface anisotropy originated in the frustrated shell spins, as observed for example in hollow FiM nanoparticles.[43,56] On the other hand, it is noteworthy that assuming that the systems present an equivalent morphology, core size and shell thickness, the overall magnetic behavior cannot be explained by considering solely the effects of the Zn doping on the properties of the ferrite. Even if the introduction of Zn into the ferrite diminishes the coercivity, it fails to explain the variation of H_{EB} with x and the H_C values, which are much larger than their bulk counterparts. In addition, the small variation of M_S measured, between 28–38 emu g_{NPs}^{-1}, cannot account for such results. Instead, the remarkable increase in H_C for our core/shell nanoparticles can be explained by considering the AFM/FiM interface coupling that provides an additional source of anisotropy, as has been found in similar bimagnetic systems.[24,30,36,57–59] Following, some considerations about the interface coupling can be helpful to understand the obtained results. The maximum observed in the H_{EB} dependence on the Zn concentration is ascribed to the presence of different coupling regimes promoted by the relationship between the interface exchange coupling energy E_{EX} and the anisotropy energy of the antiferromagnet, the latter given by $K_{AFM}V_{AFM}$, where K_{AFM} and V_{AFM} are the anisotropy constant and the volume of the AFM core, respectively.[10,15] The negligible H_{EB} found for $x = 0$ ($CoO/CoFe_2O_4$) and the remarkable increase in the H_C, which is 21.5 kOe in the present case and increasing up to 31.5 kOe for smaller particles,[37] are consistent with $E_{EX} > K_{AFM}V_{AFM}$.[36] In contrast, when the shell is doped with Zn^{2+} the system exhibits both an increased H_C and exchange-biased loops, which can be explained by considering $E_{EX} < K_{AFM}V_{AFM}$. Moreover, the strong dependence of H_{EB} on the Zn content evidences its determinant role in the EB properties.

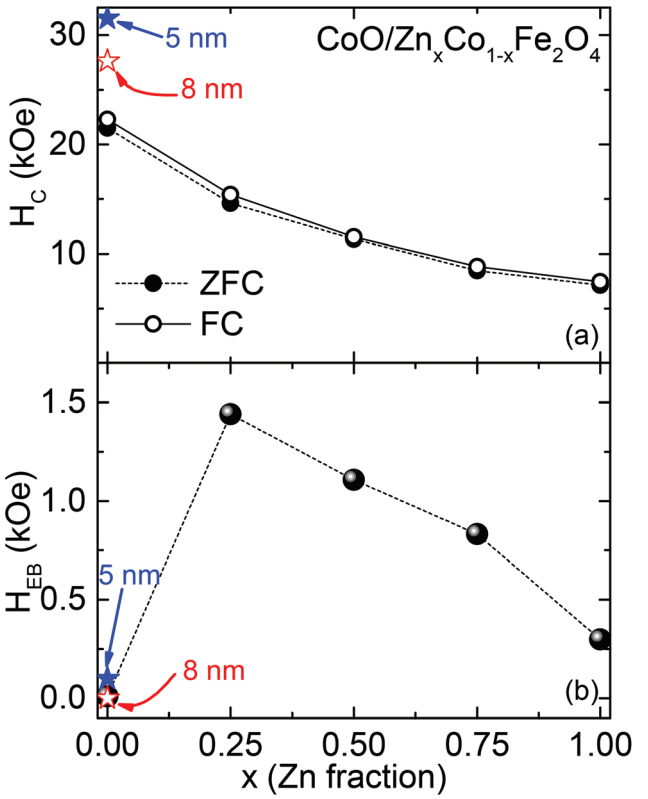

Fig. 5 (a) Zero-field-cooled and field-cooled (from 310 K with 10 kOe) H_C and (b) H_{EB} of $CoO/Co_{1-x}Zn_xFe_2O_4$ ($x = 0$–1) core/shell nanoparticles (samples Zn-x) measured at 5 K. For comparison, ZFC H_C and H_{EB} values for 5 and 8 nm $CoO/CoFe_2O_4$ from ref. 37 are shown.

Table 2 Summary of the magnetic characterization of $CoO/Zn_xCo_{1-x}Fe_2O_4$ nanoparticles: nominal Zn fraction (x_{NOM}), ZFC coercive field (H_C^{ZFC}), FC coercive field (H_C^{FC}) and exchange bias field (H_{EB}) measured at 5 K, as well as mean blocking temperature estimated from the temperature variation of the magnetization $\langle T_B \rangle$, interface exchange-coupling energy (E_{EX}^{surf}) and fraction of pinned uncompensated AFM spins (n)

Sample	x_{NOM}	H_C^{ZFC} (kOe)	H_C^{FC} (kOe)	H_{EB} (kOe)	$\langle T_B \rangle$ (K)	E_{EX}^{surf} (erg cm^{-2})	n
Zn-0	0	21.5	22.3	0.01	>300	—	—
Zn-0.25	0.25	14.6	15.4	1.44	122	0.66	0.11
Zn-0.5	0.5	11.3	11.5	1.11	112	0.49	0.08
Zn-0.75	0.75	8.5	8.8	0.83	137	0.36	0.06
Zn-1	1	7.1	7.5	0.30	123	0.19	0.03

The interplay between the interface exchange energy and the magnetic anisotropy is also manifested in the thermal stability of the magnetic moment. From the zero-field-cooled (ZFC) and field-cooled magnetization (FC) curves (shown in Fig. 6), we have obtained the energy barrier distribution $f(T_B) \sim (1/T)(d(M_{ZFC} - M_{FC})/dT)$, which accounts for the distribution of the magnetic anisotropy of the system and also for the increase in the energy barrier due to the intra- and interparticle interactions.[60] From the mean value of the $f(T_B)$ distribution we have obtained the mean blocking temperature $\langle T_B \rangle$ of each sample, as reported in Table 2. In exchange-biased nanoparticle systems, $\langle T_B \rangle$ reflects both the blocking process

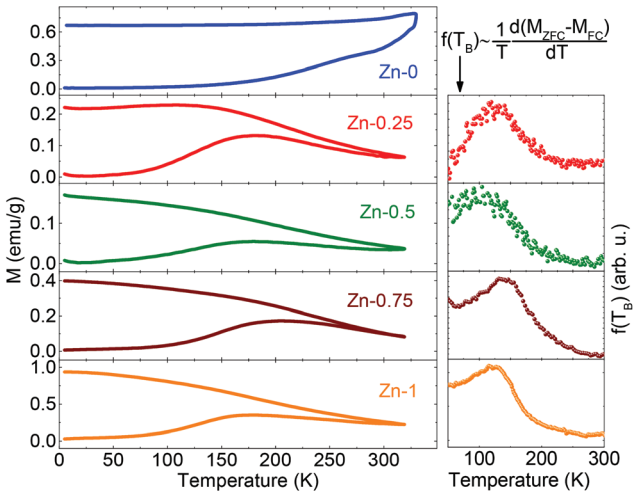

Fig. 6 Temperature dependence of the ZFC and FC magnetization of $CoO/Zn_xCo_{1-x}Fe_2O_4$ nanoparticles, measured under an applied field of 50 Oe. The distribution of blocking temperatures estimated from the measurements are shown in the right panel (note that if $\langle T_B \rangle$ > 300 K for Zn-0, then it was not possible to estimate $f(T_B)$ in this case).

and the presence of interactions and, in ideal exchange-biased nanoparticle systems, it is expected to shift up to the Néel temperature of the AFM due to the interface exchange interaction. However, in many nanostructures, the superparamagnetic behavior is observed at much lower temperatures than T_N. This is typically ascribed to the finite size effect of the AFM component that fails to pin the FiM spins as a result of its superparamagnetic relaxation.[10,34,40,61] In our system, while $\langle T_B \rangle$ is higher than room temperature for $x = 0$, it does not change significantly with the Zn doping for $x = 0.25$, 0.5, 0.75 and 1 ($\langle T_B \rangle \sim 112$ K–137 K). Such a behavior is clearly in contrast to the blocking temperatures reported for single phase $ZnFe_2O_4$ nanoparticles of a similar size which are in the range of ~15–40 K due to a reduced magnetic anisotropy of $\sim 2 \times 10^5$ erg cm^{-3}.[49] Therefore, consistent with the expected behavior for an exchange-biased system, for $x > 0$, we can relate $\langle T_B \rangle$ with the blocking temperature of the magnetically hard CoO core, which fails to pin the FiM spins above $\langle T_B \rangle$ due to its thermal fluctuation. Within this rough approximation, the magnetic anisotropy constant of the AFM phase can be estimated from the Néel model $K_{AFM}V_{AFM} = 25k_BT_B$; then, by considering a mean $T_B \sim 123$ K for $x = 0.25$–1 and a ~3 nm diameter for the AFM core, the calculations lead to $K_{AFM} \sim 3.0 \times 10^7$ erg cm^{-3}, a value in excellent agreement with previous reports.[36,61] A different situation is found for $x = 0$, where the increase in the thermal stability of the magnetic moment above T_N is ascribed to the large magnetocrystalline anisotropy of the FiM $CoFe_2O_4$ shell.[37]

By increasing the degree of complexity new variables are being introduced into the study of core/shell nanoparticles, including local variations of the anisotropy or interface interactions and the possibility of core–shell interdiffusion. It has been reported that the latter can widen the energy barrier distribution and can also affect both H_{EB} and H_C.[33,62] Although from our data we cannot discard some core/shell interdiffusion as suggested *e.g.* by the slightly lower cell parameter of the Zn–Co ferrite compared to that expected for the bulk system, the experimental results do not show any evidence of significant deterioration of the magnetic properties of the core due to this effect. In fact, the blocking temperatures of samples Zn-0.25–Zn-1 are in very good agreement with the expected anisotropy of the CoO and a remarkable enhancement of the magnetic hardness is observed for the whole system. However, it is worth mentioning that the possibility of controlling the core–shell intermixing (*e.g.* by an appropriate post-synthesis treatment) could be an interesting approach to tune the magnetic properties and certainly deserves further investigation. Moreover, given the higher coercivity and thermal stability compared to single-phase nanoparticles with similar sizes, the fact that the shell is formed by several ferrite nanograins reinforces the assumption that the overall magnetic behavior is governed by the AFM/FiM interactions. The morphology of the ferrite plays therefore a key role in determining the effective coupling between the core and shell which also affects the magnetization reversal process by promoting a greater degree of incoherent reversal, as was shown elsewhere.[23]

Even if a quantitative analysis of H_{EB} is usually difficult we can estimate, as a first approximation, the interface coupling energy by $E_{EX} = H_{EB}V_{FiM}M_S$, where V_{FiM} is the FiM volume and M_S is the saturation magnetization of the ferrite.[10] Since the morphology and size are similar for all the samples, we can consider average diameters of 11 nm and 2.7 nm for the whole nanoparticle and the core, respectively, and the experimental M_S values for the Zn–Co ferrite. Then, the surface interface energy can be calculated from the field-shifts by $E_{EX}^{surf} = E_{EX}/A_{int}$, where A_{int} is the total area of the interface. The obtained E_{EX}^{surf} values (reported in Table 2) are in agreement with the interface energies measured for other CoO-based heterostructures, which are in the range of 0.1–3.5 erg cm^{-2}.[11] Even though no significant hysteresis loop shifts are observed for the $CoO/CoFe_2O_4$ system, from our analysis an estimation of E_{EX} can be provided by the linear extrapolation of the data for $x = 0$, as shown in Fig. 7, which results in $\sim 2 \times 10^{-13}$ erg, close to the anisotropy energy of the AFM given by $K_{AFM}V_{AFM} \sim 3.1 \times 10^{-13}$ erg, with such a difference being increased with the Zn concentration.

The dependence of H_{EB} on the Zn content can be further analyzed by considering the microscopic picture and the local origin of the EB. In ref. 28, Ohldag *et al.* showed that only a fraction of the interfacial spins, *i.e.* pinned uncompensated spins, contributes effectively to the EB, as evidenced by the fact that the experimental H_{EB} values are usually lower than the theoretical predictions. These findings are summarized in a simple extension of the Meiklejohn and Bean model,[9,28] where the surface exchange energy can be calculated by $E_{EX}^{surf} = J_{EX}^{eff}S_{FiM}S_{AFM}/a_{AFM}^2$, S_{FiM} and S_{AFM} being the magnetic spins of the FiM and AFM, respectively, and a_{AFM} is the lattice parameter of the AFM. In this model, J_{EX}^{eff} is an effective exchange

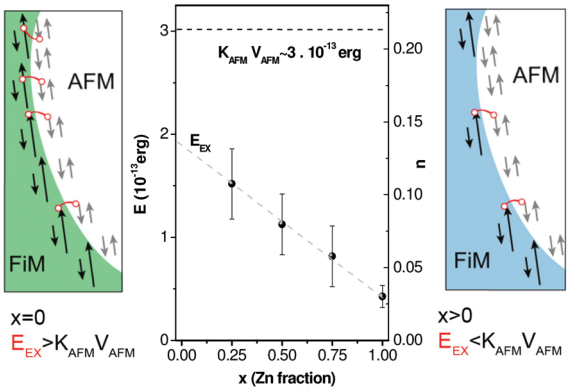

Fig. 7 Variation of the interface exchange-coupling energy (E_{EX}) and the associated fraction of pinned uncompensated spins at the interface (n, right axis) with the Zn concentration (solid line) estimated from the experimental data (circles). The horizontal dotted line indicates the anisotropy energy of the AFM core estimated from the experimental data. The left (x = 0) and right (x > 0) panels show schematically the reduction in the effective number of exchange-coupling bonds at the interface when doping the Co-ferrite with non-magnetic Zn atoms.

coupling constant given by $J_{EX}^{eff} = nJ_{EX}$, where n is the fraction of pinned uncompensated spins at the interface and J_{EX} is the exchange coupling constant at the interface. Then, by assuming $J_{EX} = J_{Co-Co}$ = 21.2 K, $S_{AFM} = S_{Co^{2+}}$ = 3/2, $S_{FiM} \approx$ 5/2 and a_{AFM} = 4.26 Å,[48] n can be estimated from the experimental data. Table 2 summarizes the calculated density of pinned spins as a function of the Zn concentration, which decreases from n = 0.11 for x = 0.25 to n = 0.03 for x = 1, in good agreement with previous studies of bimagnetic nanostructures.[25,28] The approximately linear decrease of H_{EB} and n with x, shown on the right axis of Fig. 7, is then associated with the reduction of the effective exchange coupling bonds at the interface due to the Zn doping. Therefore, the results indicate that the incorporation of non-magnetic Zn^{2+} ions into the ferrite promotes a lower exchange-coupling energy at the interface, altering the ratio between $K_{AFM}V_{AFM}$ of the CoO and E_{EX} and enabling control of the exchange bias and the anisotropy enhancement.

4. Conclusions

A systematic study of the magnetic properties of CoO/$Co_{1-x}Zn_xFe_2O_4$ (x = 0–1) core/shell nanoparticles, with analogous structural characteristics, reveals that the exchange coupling at the interface can be tuned by the introduction of non-magnetic Zn atoms into the ferrite shell. By modifying the density of the available exchange bonds at the interface, the relationship between the interface exchange-coupling energy and the anisotropy energy of the AFM is altered. As a consequence, the magnetization reversal mechanism changes from a rigid coupling regime with enhanced H_C for x = 0 to an exchange-biased regime for x > 0, as reflected in the non-monotonic dependence of H_{EB} on the amount of Zn. In summary, we propose a new approach for tuning the coercivity and exchange bias in AFM/FiM core/shell nanostructures and our results provide a novel strategy for designing hybrid exchange-coupled nanostructured materials with controlled magnetic properties.

Acknowledgements

The authors thank ANPCyT and CONICET Argentina for support through Grant No. PICT-2015-0883 and Grant No. PIP 112-20110100519, respectively and UNCuyo for support through Grant No. 06/C527 and 06/C528.

References

1 S. Parkin, X. Jiang, C. Kaiser, A. Panchula, K. Roche and M. Samant, *Proc. IEEE*, 2003, **91**, 661–680.
2 J. Kools, *IEEE Trans. Magn.*, 1996, **32**, 3165–3184.
3 E. Kneller and R. Hawig, *IEEE Trans. Magn.*, 1991, **27**, 3588–3600.
4 E. E. Fullerton, J. S. Jiang and S. D. Bader, *J. Magn. Magn. Mater.*, 1999, **200**, 392–404.
5 V. Skumryev, S. Stoyanov and Y. Zhang, *Nature*, 2003, **423**, 19–22.
6 A. López-Ortega, M. Estrader, G. Salazar-Alvarez, A. G. Roca and J. Nogués, *Phys. Rep.*, 2015, **553**, 1–32.
7 J. Lee, J. Jang, J. Choi, S. Moon, S. Noh, J. Kim, J. Kim, I. Kim, K. Park and J. Cheon, *Nat. Nanotechnol.*, 2011, **6**, 418–422.
8 H. Zeng, J. Li, J. Liu, Z. Wang and S. Sun, *Nature*, 2002, **420**, 395–398.
9 W. H. Meiklejohn and C. P. Bean, *Phys. Rev.*, 1956, **102**, 1413.
10 J. Nogués, J. Sort, V. Langlais, V. Skumryev, S. Suriñach, J. Muñoz and M. Baró, *Phys. Rep.*, 2005, **422**, 65–117.
11 J. Nogués and I. K. Schuller, *J. Magn. Magn. Mater.*, 1999, **192**, 203–232.
12 K. Takano, R. Kodama, A. Berkowitz, W. Cao and G. Thomas, *Phys. Rev. Lett.*, 1997, **79**, 1130.
13 A. Dobrynin, D. Ievlev, K. Temst, P. Lievens, J. Margueritat, J. Gonzalo, C. N. Afonso, S. Zhou, A. Vantomme, E. Piscopiello and G. Van Tendelloo, *Appl. Phys. Lett.*, 2005, **87**, 012501.
14 Q. K. Ong, A. Wei and X.-M. Lin, *Phys. Rev. B: Condens. Matter*, 2009, **80**, 134418.
15 F. Radu and H. Zabel, *Magnetic Heterostructures*, Springer, Berlin, Heidelberg, 2008, vol. 227, pp. 97–184.
16 S. Sun, C. Murray, D. Weller, L. Folks and A. Moser, *Science*, 2000, **287**, 1989–1992.
17 T. Hyeon, S. S. Lee, J. Park, Y. Chung and H. B. Na, *J. Am. Chem. Soc.*, 2001, **123**, 12798–12801.
18 J. van Embden, A. S. R. Chesman and J. J. Jasieniak, *Chem. Mater.*, 2015, **27**, 2246–2285.
19 S. Chandra, H. Khurshid, W. Li, G. C. Hadjipanayis, M. H. Phan and H. Srikanth, *Phys. Rev. B: Condens. Matter*, 2012, **86**, 014426.

20 W. Baaziz, B. P. Pichon, C. Lefevre, C. Ulhaq-Bouillet, J.-M. Greneche, M. Toumi, T. Mhiri and S. Bégin-Colin, *J. Phys. Chem. C*, 2013, **117**, 11436–11443.
21 H. Zeng, J. Li, Z. L. Wang, J. P. Liu and S. Sun, *Nano Lett.*, 2004, **4**, 187–190.
22 M. Estrader, A. López-Ortega, S. Estradé, I. V. Golosovsky, G. Salazar-Alvarez, M. Vasilakaki, K. N. Trohidou, M. Varela, D. C. Stanley, M. Sinko, M. J. Pechan, D. J. Keavney, F. Peiró, S. Suriñach, M. D. Baró and J. Nogués, *Nat. Commun.*, 2013, **4**, 2960.
23 G. C. Lavorato, D. Peddis, E. Lima Jr., H. E. Troiani, E. Agostinelli, D. Fiorani, R. D. Zysler and E. L. Winkler, *J. Phys. Chem. C*, 2015, **119**, 15755–15762.
24 E. Lima, E. L. Winkler, D. Tobia, H. E. Troiani, R. D. Zysler, E. Agostinelli and D. Fiorani, *Chem. Mater.*, 2012, **24**, 512–516.
25 G. Salazar-Alvarez, J. Sort, S. Suriñach, M. D. Baró and J. Nogués, *J. Am. Chem. Soc.*, 2007, **129**, 9102–9108.
26 G. Salazar-Alvarez, H. Lidbaum, A. López-Ortega, M. Estrader, K. Leifer, J. Sort, S. Suriñach, M. D. Baró and J. Nogués, *J. Am. Chem. Soc.*, 2011, **133**, 16738–16741.
27 H. Khurshid, S. Chandra, W. Li, M. H. Phan, G. C. Hadjipanayis, P. Mukherjee and H. Srikanth, *J. Appl. Phys.*, 2013, **113**, 17B508.
28 H. Ohldag, A. Scholl, F. Nolting, E. Arenholz, S. Maat, A. T. Young, M. Carey and J. Stöhr, *Phys. Rev. Lett.*, 2003, **91**, 017203.
29 X. Sun, N. F. Huls, A. Sigdel and S. Sun, *Nano Lett.*, 2012, **12**, 246–251.
30 X. Liu, B. P. Pichon, C. Ulhaq, C. Lefèvre, J.-M. Grenèche, D. Bégin and S. Bégin-Colin, *Chem. Mater.*, 2015, **27**, 4073–4081.
31 E. Lottini, A. López-Ortega, G. Bertoni, S. Turner, M. Meledina, G. Tendeloo, C. Van de Julián Fernández and C. Sangregorio, *Chem. Mater.*, 2016, **28**, 4214–4222.
32 M. Sytnyk, R. Kirchschlager, M. I. Bodnarchuk, D. Primetzhofer, D. Kriegner, H. Enser, J. Stangl, P. Bauer, M. Voith, A. W. Hassel, F. Krumeich, F. Ludwig, A. Meingast, G. Kothleitner, M. Kovalenko and W. Heiss, *Nano Lett.*, 2013, **13**, 586–593.
33 E. Skoropata, R. Desautels, C.-C. Chi, H. Ouyang, J. Freeland and J. van Lierop, *Phys. Rev. B: Condens. Matter*, 2014, **89**, 024410.
34 O. Iglesias, A. Labarta and X. Batlle, *J. Nanosci. Nanotechnol.*, 2008, **8**, 2761–2780.
35 M. Vasilakaki, K. N. Trohidou and J. Nogués, *Sci. Rep.*, 2015, **5**, 9609.
36 E. L. Winkler, E. Lima, D. Tobia, M. E. Saleta, H. E. Troiani, E. Agostinelli, D. Fiorani and R. D. Zysler, *Appl. Phys. Lett.*, 2012, **101**, 252405.
37 G. C. Lavorato, E. Lima Jr., D. Tobia, D. Fiorani, H. E. Troiani, R. D. Zysler and E. L. Winkler, *Nanotechnology*, 2014, **25**, 355704.
38 S. Sun and H. Zeng, *J. Am. Chem. Soc.*, 2002, **124**, 8204–8205.
39 G. Lavorato, E. Lima, H. Troiani, R. Zysler and E. Winkler, *J. Alloys Compd.*, 2015, **633**, 333–337.
40 G. Lavorato, E. Winkler, A. Ghirri, E. Lima Jr., D. Peddis, H. E. Troiani, D. Fiorani, E. Agostinelli, D. Rinaldi and R. D. Zysler, *Phys. Rev. B: Condens. Matter*, 2016, **94**, 054432.
41 R. Arulmurugan, G. Vaidyanathan, S. Sendhilnathan and B. Jeyadevan, *J. Magn. Magn. Mater.*, 2006, **303**, 131–137.
42 S. Kumar, V. Singh, S. Aggarwal, U. K. Mandal and R. Kotnala, *J. Magn. Magn. Mater.*, 2012, **324**, 3683–3689.
43 H. Khurshid, P. Lampen-Kelley, Ò. Iglesias, J. Alonso, M.-H. Phan, C.-J. Sun, M.-L. Saboungi and H. Srikanth, *Sci. Rep.*, 2015, **5**, 15054.
44 A. Dreyer, A. Feld, A. Kornowski, E. D. Yilmaz, H. Noei, A. Meyer, T. Krekeler, C. Jiao, A. Stierle, V. Abetz, H. Weller and G. A. Schneider, *Nat. Mater.*, 2016, **15**, 522–528.
45 M. V. Limaye, S. B. Singh, S. K. Date, D. Kothari, V. R. Reddy, A. Gupta, V. Sathe, R. J. Choudhary and S. K. Kulkarni, *J. Phys. Chem. B*, 2009, **113**, 9070–9076.
46 D. Amara, I. Felner, I. Nowik and S. Margel, *Colloids Surf., A*, 2009, **339**, 106–110.
47 K. Yang, H. Peng, Y. Wen and N. Li, *Appl. Surf. Sci.*, 2010, **256**, 3093–3097.
48 J. Coey, *Magnetism and Magnetic Materials*, Cambridge University Press, 2010.
49 S. Bullita, A. Casu, M. F. Casula, G. Concas, F. Congiu, A. Corrias, A. Falqui, D. Loche and C. Marras, *Phys. Chem. Chem. Phys.*, 2014, **16**, 4843–4852.
50 Z. Ž. Lazarević, Č. Jovalekić, V. N. Ivanovski, A. Rečnik, A. Milutinović, B. Cekić and N. Ž. Romčević, *J. Phys. Chem. Solids*, 2014, **75**, 869–877.
51 G. Goya and H. Rechenberg, *J. Magn. Magn. Mater.*, 1999, **196–197**, 191–192.
52 C. Yao, Q. Zeng, G. F. Goya, T. Torres, J. Liu, H. Wu, M. Ge, Y. Zeng, Y. Wang and J. Z. Jiang, *J. Phys. Chem. C*, 2007, **111**, 12274–12278.
53 H. Huang, Y. Zhang, Z. Huang, Z. Kou, X. Yuan, Z. Ren, Y. Zhai, J. Du and H. Zhai, *J. Appl. Phys.*, 2015, **117**, 17E711.
54 V. Mameli, A. Musinu, A. Ardu, G. Ennas, D. Peddis, D. Niznansky, C. Sangregorio, C. Innocenti, N. T. Thanh and C. Cannas, *Nanoscale*, 2016, **8**, 10124–10137.
55 F. Gözüak, Y. Köseoglu, A. Baykal and H. Kavas, *J. Magn. Magn. Mater.*, 2009, **321**, 2170–2177.
56 E. De Biasi, E. Lima Jr., J. M. Vargas, R. D. Zysler, J. Arbiol, A. Ibarra, G. F. Goya and M. R. Ibarra, *Mater. Res. Express*, 2015, **2**, 105001.
57 N. Fontaíña Troitiño, B. Rivas-Murias, B. Rodríguez-González and V. Salgueiriño, *Chem. Mater.*, 2014, **26**, 5566–5575.
58 S. Sharma, J. Vargas, K. Pirota, S. Kumar, C. Lee and M. Knobel, *J. Alloys Compd.*, 2011, **509**, 6414–6417.
59 D. Kavich, J. Dickerson, S. Mahajan, S. Hasan and J.-H. Park, *Phys. Rev. B: Condens. Matter*, 2008, **78**, 174414.
60 J. Dormann, F. D'Orazio, F. Lucari, E. Tronc, P. Prené, J. Jolivet, D. Fiorani, R. Cherkaoui and M. Noguès, *Phys. Rev. B: Condens. Matter*, 1996, **53**, 14291–14297.
61 J. B. Tracy, D. N. Weiss, D. P. Dinega and M. G. Bawendi, *Phys. Rev. B: Condens. Matter*, 2005, **72**, 064404.
62 E. Skoropata, T. T. Su, H. Ouyang, J. W. Freeland and J. Van Lierop, *J. Appl. Phys.*, 2015, **117**, 3–7.

